CFD SIMULATIONS OF AERODYNAMIC FLOWS WITH A PRESSURE-BASED METHOD

F. R. Menter*, P.F. Galpin*, T. Esch*, M. Kuntz*, C. Berner**
***ANSYS Inc., ** French-German Research Institute ISL**

Keywords: *CFD, Numerical method, Pressure based, Mach number, Aerodynamics*

Abstract

The paper describes the numerical method behind the general-purpose code CFX-5. It will concentrate on the formulation of the solver for different Mach number flows while using a pressure-based formulation. Numerous aeronautical examples will be shown, from incompressible flows to flows at high supersonic speeds.

1 Introduction

CFD based on the Reynolds Averaged Navier Stokes (RANS) equations is now widely used in the aeronautical industry during the design process. While a large number of studies are concerned with classical aerodynamic simulations at transonic speeds, an increasing number of auxiliary simulations are required to optimize the entire aircraft. This includes flows at low speeds (take-off and landing, cabin climate), multi-phase flows (icing) as well as "multi-physics" applications (fluid-structure coupling, aerodynamic noise generation, radar signature). Historically, different codes are used for the different applications. The auxiliary simulations are mostly based on general-purpose codes, while in-house or special purpose codes are used for the external aerodynamics. However, an increasing number of applications require the combination of generality with a high degree of numerical and modelling accuracy. It is therefore essential that general-purpose codes provide a level of accuracy and numerical performance satisfying the requirements of aeronautical design engineers.

Aerodynamics codes are typically built on density-based formulations, which have evolved from methods developed for the solution of the Euler equations [1][2][3]. They are mostly optimized for tight shock resolution and non-oscillatory behavior near extrema.

On the other hand, general-purpose industrial codes are generally built on pressure-based formulations like the SIMPLE or SIMPLEC schemes see e.g. Ref. [4] or more recent method like those given by Rhie and Chow [5] or [6][7]. These codes typically offer a much wider range of physical models and boundary conditions and can be applied to complex, "multi-physics" problems, involving the coupling of different CAE tools.

One of the challenges in formulating a general-purpose code lies in the requirement of covering the entire Mach number range from incompressible to supersonic and even hypersonic flows. In addition, the numerical scheme must be able to support multi-phase flows (Euler-Euler formulation) and flows with chemical reactions, both of which can show large variations in fluid properties, particularly in the fluid density. While density-based methods are well suited for compressible single-phase flows, they quickly deteriorate if large regions of the flow field are at low speed, or if fluids with strongly different properties are involved. While preconditioning techniques [8][9] can in principle extend the range of density-based formulations into these flow regimes, they had so far little impact on general-purpose industrial flow solvers.

Pressure-based formulations on the other hand can treat incompressible flows with high numerical efficiency, but specific considerations

are required for their extension to compressible flows. In addition, the accurate simulation of aerodynamic flows requires the use of highly optimized turbulence models [10][11] and their integration through the viscous sublayer. The classical combination of the k-ε model with wall functions, which has for long been the paradigm in general purpose codes, can not satisfy the accuracy requirements in the aeronautical community. While more advanced turbulence models are easily implemented, the need to integrate them robustly on "low-Re" grids requires numerical formulations, which can handle the resulting high aspect ratios of the near wall cells.

In section 2, the numerical formulation of the general-purpose code CFX-5 will be laid out. One of the central aspects of this method is the use of a coupled formulation for the mass and momentum equations. Based in the authors experience with the more classical segregated approach, the implicit coupling is essential, as it generally accelerates convergence, avoids convergence difficulties for compressible flows and can naturally handle high-aspect ratio cells. In addition, a short description of the algebraic multi-grid (AMG) solver used for solving the linear equations will be given.

In section 3, different generic test cases will be shown. They cover a range of Mach numbers and their purpose is to demonstrate the numerical performance as well as the accuracy of the method.

In section 4, some examples of complex simulations of aerodynamic configurations will be given. Again, the emphasis is on numerical performance for a variety of Mach and Reynolds numbers. All test cases have been computed with the SST turbulence model [11].

2 Numerical Method

2.1 Basic equations

The relevant equations of motion for aerodynamic flows are the mass, momentum and energy equations:

$$\frac{\partial \rho}{\partial t} + \frac{\partial}{\partial x_j}\left(\rho u_j\right) = 0 \qquad (1)$$

$$\frac{\partial}{\partial t}\left(\rho u_i\right) + \frac{\partial}{\partial x_j}\left(\rho u_j u_i\right) = -\frac{\partial P}{\partial x_i} + \frac{\partial \tau_{ij}}{\partial x_j} + S_{u_i}$$

$$\frac{\partial}{\partial t}\left(\rho H - P\right) + \frac{\partial}{\partial x_j}\left(\rho u_j H\right) = \frac{\partial}{\partial x_j}\left(k\frac{\partial T}{\partial x_j}\right) - \frac{\partial}{\partial x_j}\left(u_j \tau_{ij}\right) + S_T$$

where ρ is density, u_i is velocity, P is pressure, μ is the fluid viscosity, H is total enthalpy $H = h + u_i u_i / 2$, h is the static enthalpy, T is temperature and τ_{ij} is the stress tensor. These equations are supplemented by an equation of state, $\rho = \rho(P,T)$, a stress-strain relation for τ_{ij} as a function of viscosity, μ, and the strain rate, the thermal conductivity, k, and a thermodynamic enthalpy definition, $h = h(P,T)$. For turbulent flows, an eddy-viscosity is typically added and the equations are solved for the Reynolds averaged quantities. The general form of the equations stays the same.

2.2 Discretization of the equations

The present method uses an implicit pressure-based formulation, where the primary dependent variables are (P, u_i, H). This is a typical choice for general-purpose codes, as it allows an efficient treatment of incompressible flows, which are frequently encountered in industrial CFD simulations. Provisions, which have to be taken to ensure a proper coupling between the pressure and the velocity fields for flows with strong variations in density, will be described below.

The control volume is constructed around an element vertex as the dual element mesh, as shown in Figure 1. The procedure is the same for all element types (hex, tet, wedge, pyramid).

The numerical accuracy of the simulation is determined by the accuracy of the representation of the surface integrals (fluxes) at the integration points in terms of the nodal variables.

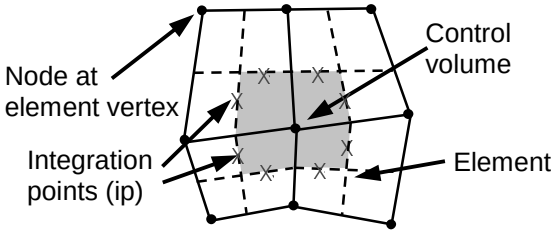

Figure 1: Mesh arrangement and terminology for dual mesh.

The equations are discretized by integrating over a finite volume. The discrete integral form of the mass, momentum and energy equations is:

$$\rho V\left(\frac{\rho-\rho^{o}}{\Delta t}\right)+\sum_{ip}\left(\rho u_j \Delta n_j\right)_{ip}=0 \qquad (2)$$

$$\rho V\left(\frac{u_i-u_i^{o}}{\Delta t}\right)+\sum_{ip} m_{ip}(u_i)_{ip}=\sum_{ip}(P\Delta n_i)_{ip}+\sum_{ip}\left(\mu_{eff}\left(\frac{\partial u_i}{\partial x_j}+\frac{\partial u_j}{\partial x_i}\right)\Delta n_j\right)_{ip}+\overline{S_{u_i}}V$$

$$\rho V\left(\frac{(H-P/\rho)-(H^{o}-P^{o}/\rho^{o})}{\Delta t}\right)+\sum_{ip} m_{ip}H_{ip}=\sum_{ip}\left(k_{eff}\frac{\partial T}{\partial x_j}\Delta n_j\right)_{ip}+\overline{S_{\phi}}V$$

where $(\Delta n_j)_{ip}$ is the local surface vector at the integration point *(ip)* location and m_{ip} is the mass flow through the (*ip)* surface of the control volume [12]. Conservation is guaranteed numerically, by ensuring that each surface flux is evaluated once, uniquely, per (*ip)*.

All equations are treated implicitly to avoid time-step limitations. For the transient term, a 1st order or 2nd order backward Euler formulation is employed.

The diffusion terms are evaluated by computing gradient coefficients at each (*ip)* location in terms of derivatives of classical element shape functions [13]. This approach is accurate and ensures a compact implicit operator.

Advection terms are more critical and are evaluated by any of a number of schemes. The default scheme provides a second order accurate formulation for advection, based on an upwind-biased approach called high-resolution, similar to the approach described in [14].

$$\phi_{ip}=\phi_P+\beta\underline{(\nabla\phi)}_{ip}.\Delta\vec{r}_{ip} \qquad (3)$$

The advected (*ip)* value, ϕ_{ip}, is computed as the upwind nodal value, ϕ_P, plus a 1st derivative correction based on the distance from the upstream node to the (*ip)* location, $\Delta\vec{r}_{ip}$, in order to obtain a 2nd order accurate numerical estimate for ϕ_{ip}. The scaling factor, β, can be used to reduce the accuracy near extrema to 1st order to avoid non-physical over- or undershoots. In the implicit part, only the first order upwind terms are considered. The mass flow m_{ip} is lagged from the previous time step. The scheme is non-oscillatory for scalars, but does not guarantee strict monotonic behavior for coupled systems because the advection model is applied independently to each advected component ($u_{j,ip}, H_{ip}, \rho_{ip}$). Such oscillations are small and proven to not be problematic in practice.

As with all terms in divergence form, the mass divergence term is converted to a surface integral:

$$\dot{m}_{ip}=\rho_{ip}u_{j,ip}\Delta n_{j,ip} \qquad (4)$$

The density is computed like any other "advected" variable, and the standard high-resolution scheme is applied:

$$\rho_{ip}=\rho_P+\beta\underline{(\nabla\rho)}_{ip}.\Delta\vec{r}_{ip} \qquad (5)$$

This upwind biased estimate remains stable and 2nd order accurate even when the flow is significantly compressible, similar to advected quantities in the momentum and energy equations.

In order to prevent high-frequency pressure oscillations, the 4th order pressure smoothing of Rhie and Chow [5] is employed. It computes an estimate for $u_{j,ip}$ using a simplified momentum equation centered around the (*ip)* face. The control volume momentum equation at the point (*ip)* can symbolically be written in the form:

$$u_{ip} = \hat{u}_{ip} + d_{ip}\left(\frac{\Delta p}{\Delta x}\right)_{ip} \qquad (6)$$

where $\hat{u}_{ip}$ represents all terms in the momentum equation except the pressure term, and d_{ip} is the resulting scaling factor between the nodal velocity and the pressure gradient [5]. Estimates of $\hat{u}_{ip}$ and d_{ip} are obtained by linear interpolation of the surrounding nodal "values". The local pressure gradient at the (*ip)* location is evaluated using element based shape function derivatives. After re-arrangement and simplification, the resulting expression for the $u_{j,ip}$ velocity in the mass equation divergence term is as follows:

$$u_{j,ip} = \bar{u}_j + \bar{d}\left(\left.\frac{\partial P}{\partial x_j}\right|_{ip} - \left.\frac{\partial P}{\partial x_j}\right|_{N}\right) \qquad (7)$$

where $\bar{u}_j$ is a linear interpolation of the nodal velocities, $\bar{d}$ is a linear interpolation of the nodal p-V scaling factors and the term in braces is the difference between the local and average nodal pressure gradients. This evaluation of $u_{j,ip}$ has the desired properties of a 2nd order accurate interpolation that is sensitive to the pressure gradient, based on the local flow physics (local momentum equation).

Equally important for the implicit method is the linearization of the ρu product. First the ρu product is expanded by Newton-Raphson linearization:

$$(\rho u) \approx \rho^n u^o + \rho^o u^n - \rho^o u^o \qquad (8)$$

where superscript *n* refers to the new (implicit) and *o* is the old (lagged) time level. This linearization ensures reliable convergence for the full range of Mach numbers [14].

Lastly, the equation of state for density is differentiated in order to obtain an implicit expression for ρ^n in terms of pressure:

$$\rho^n = \rho^o + \frac{\partial \rho}{\partial p}\left(p^n - p^o\right) \qquad (9)$$

The supplied equation of state is used to compute the derivative $\frac{\partial \rho}{\partial p}$, and the previously defined high-resolution advection scheme determines which nodal pressures remain implicit .

2.3 Linear Solver

The simulation progresses by repeated solutions of the linearized control volume equation set, once per timestep for steady state simulations, or several times per timestep (to resolve non-linear effects) for transient simulations.

One of the requirements for an industrial aeronautics code is an essentially linear increase in solver effort with the number of cells *n*, even when the equations are numerically stiff (e.g. due to high aspect ratio elements found in boundary layer regions). A coupled algebraic multigrid (AMG) [15][16] solver is used to ensure such a scaling. An incomplete lower-upper (ILU0) solver is employed as a smoother. In contrast to a FAS multigrid [17], the AMG operates only on the linear system of equations. It does not require the explicit geometric generation of a sequence of coarser grids, but simply adds individual control volume equations to form larger control volumes. The inter-equation relative coefficient strengths are measured to determine how the equations should be combined to form each coarse grid.

Because the original equations are conservative control volume balances, each coarse grid equation block remains conservative. A sequence is followed beginning with the formation of the coarse grid equations (restriction), ILU0 smoothing on the coarse grid and injection of these corrections back to the next fine grid equations (prolongation). The process repeats through a fixed cycle (W-cycle). On the very coarsest mesh level (100 or less equations) a direct solver is applied to ensure the correct absolute levels of all solved-for variables.

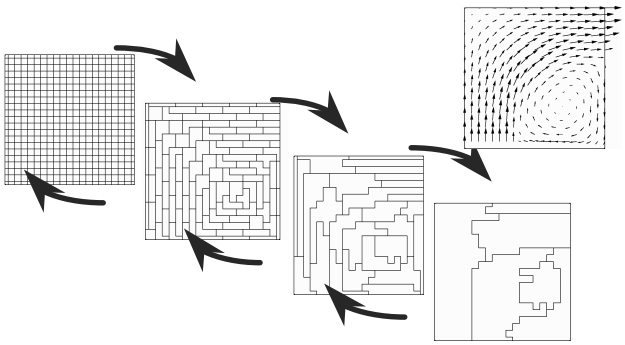

Figure 2: Sequence of coarse virtual grids for 2D circulating flow.

Figure 2 illustrates the fine to coarse grid mesh sequence the AMG solver determines for a simple 2-D flow. The effect of the flow physics on the multigrid blocking is clearly seen.

3 Generic Test cases

In the following section, results for generic test cases will be shown. They have been selected for demonstrating the codes performance for flows at various Mach numbers, with particular emphasis on flows with shock waves. Although some comparisons with experimental data will be presented, the main thrust is on the numerical performance.

3.1 Generic supersonic inlet

The first test case is the generic supersonic inlet geometry shown in Figure 3. It is a two-dimensional set-up. An oblique shock is formed from the leading edge of the geometry, followed by an isentropic expansion in the diverging section. Simulations have been performed for three different Mach numbers (Ma=5, 10, 20) and for three different grids (90×70×2; 180×140×2, 360×280×2).

Figure 4 shows convergence plots for the three grids and a Mach number of 10. It can be seen that the simulation converges in 140 iterations. The same holds true for the lower (Ma = 5) and the higher Mach number (Ma = 20).

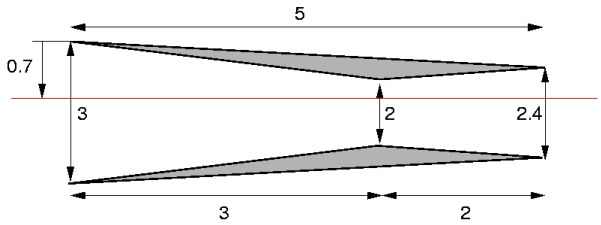

Figure 3: Geometry of the generic hypersonic inlet.

Figure 5 shows the Mach number distribution on the red line indicated in Figure 3 for the freestream Mach number Ma=10. The simulations show a close agreement with the exact solution. As expected, the method requires 3-4 cells to resolve the shock (note however that the grid line is not normal to the shock). It can also be seen that an undershoot appears behind the shock, which is however damped out quickly. This behavior is most likely a result of the higher order pressure derivatives appearing in the Rhie and Chow formulation. Similar to density-based methods using artificial viscosity formulations, it might be required to include only the second pressure derivative and avoiding the fourth derivative at shock locations. From a practical standpoint it seems be of limited consequence, as the oscillation is confined and does not affect overall accuracy and convergence.

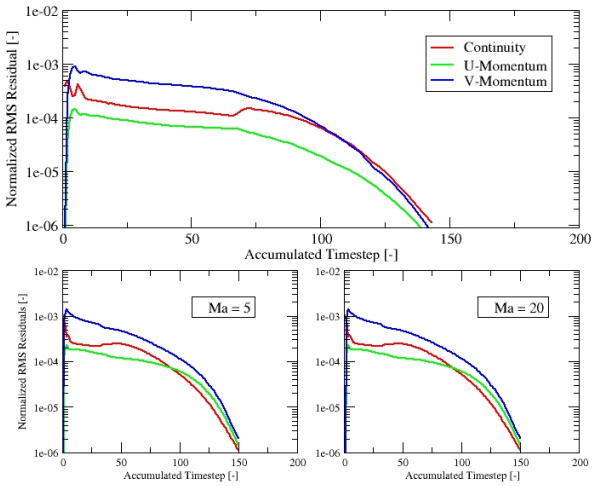

Figure 4: Convergence behavior of the momentum equations for the Ma= 5, 10 and 20 generic inlet flow.

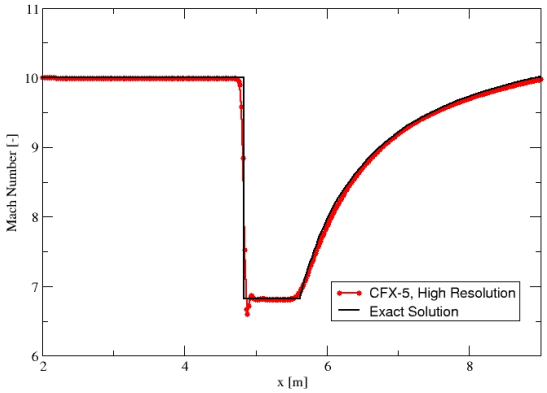

Figure 5: Mach number distribution along the inlet. Comparison between numerical data and exact inviscid theory.

3.3 Flow over flare

The next test case is a mixed laminar/turbulent hypersonic flow over a cylinder-flare. This test case was selected by the AGARD=FDP Working Group 18 as a validation case [18].

The model consists of a 0.25 m long hollow cylinder with a sharp leading edge. At the end of the cylinder a 35° flare is attached (Figure 6). The freestream conditions for this case are Ma_∞=5.01, T_∞=83.056 K, T_w=300K, Cp=1004 J/kg/K, γ=1.4.

The simulations were performed on three different grids (98×38×2, 196×76×2, 392×152×2). Grid independency was achieved on the medium grid. The maximum y^+ value on the medium grid was 0.87.

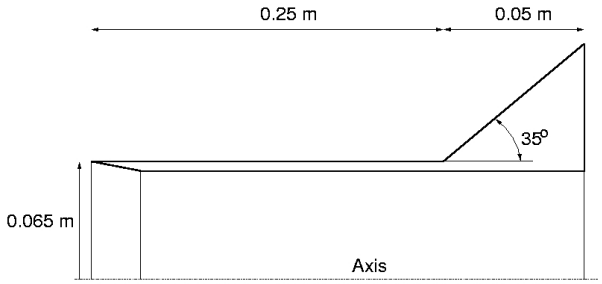

Figure 6: Hollow-cylinder flare geometry

Figure 7 shows the momentum convergence plots for the medium grid. It can be seen that the simulation converged in 300 iterations to a normalized RMS residual of below 10^{-4}.

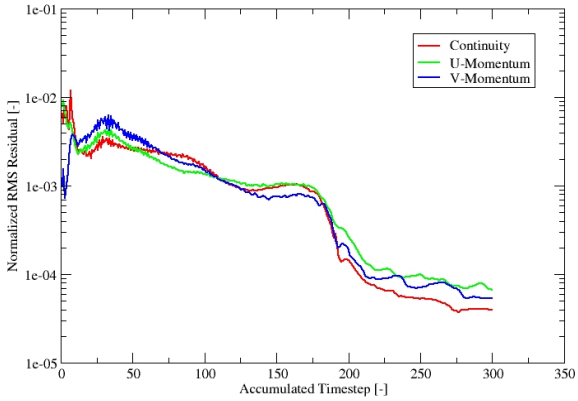

Figure 7: Convergence behavior of the momentum equations for the flare flow.

Figure 8 shows the pressure distributions for the fully turbulent simulation and the transitional simulation [19] in comparison to the experimental data. The agreement between the experimental data and the simulation with the transition model is very good. The pressure distribution for the fully turbulent simulation shows a slightly larger flow separation ahead of the flare.

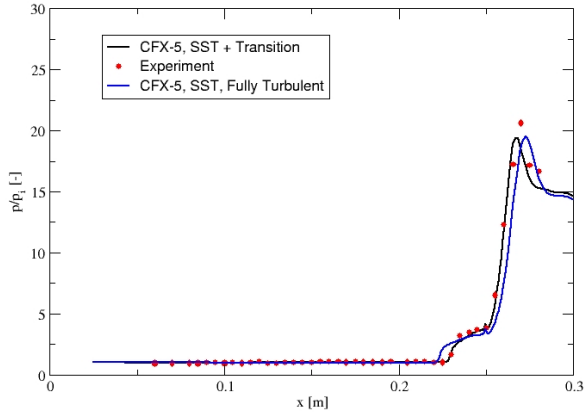

Figure 8: Wall pressure distribution along the cylinder and flare.

Figure 9 shows the Stanton number distribution along the cylinder and flare. The simulation with the transition model shows a very good agreement with the experimental data, although the peak value and the location of

the maximum of the local heat flux are slightly underestimated. The fully turbulent simulation fails to properly predict the heat flux ahead of the transition point and also underestimates the Stanton number peak more strongly than the simulation with the transition model. The inclusion of the transition model has limited effect on the numerical performance of the method.

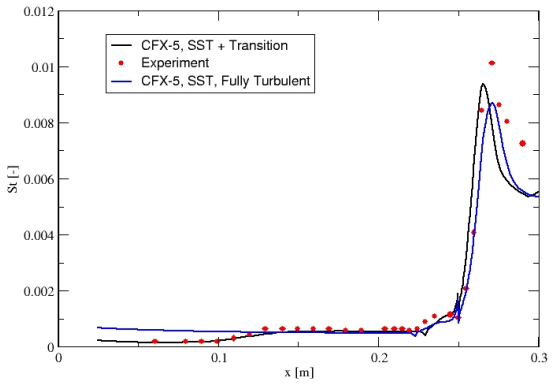

Figure 9: Stanton number distribution along cylinder and flare. Comparison between transitional and fully turbulent simulation.

4 Aeronautical Applications

The following test cases show the performance of the code for complex aeronautical applications.

4.1 Flow over low-speed forward swept-wing configuration

The geometry of the present test case is shown in Figure 10. It is a generic fighter aircraft geometry with a forward-swept wing design, which has been investigated experimentally by Breitsamter et al. [20][21]. The flow conditions for this case are: Ma_∞ =0.118, Re=0.46x10^6, α=0-45°. Grids for the simulations are curtsey of EADS military aircraft [22]. The flow serves as a test case for low sped flows.

Grids with three different levels of resolution have been evaluated. Due to the symmetry of the body, only half of the geometry was computed. Table 1 shows the grid information and the numerical requirements for the different simulations. Table 1 also shows the CPU times for a Fujitsu/Siemens PC cluster with 1600 Mhz Athlon processors. It can be seen that the numerical effort scales almost linearly with the grid size, independent of the number of parallel CPUs. This is a result of the coupled solver in combination with the AMG described in section 2.

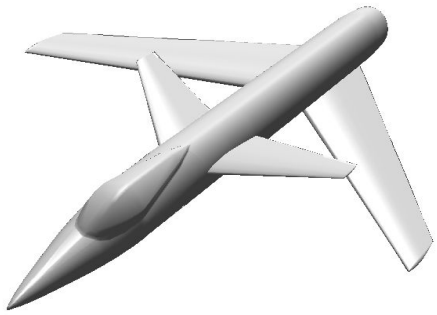

Figure 10: Geometry of forward-swept wing configuration.

Grid	No. Cells	Iter.	No. CPUs	Wall Clock	Total CPU
Fine	10 x10^6	100	26	8h	164h
Medium	1.2 x10^6	100	4	5h	18h
Coarse	0.15x10^6	100	2	1h	2h

Table 1: Information on grid and numerical effort for forward swept wing simulations

All simulations have been run for ~100 iterations, which has proven sufficient for converging the residual and the forces.

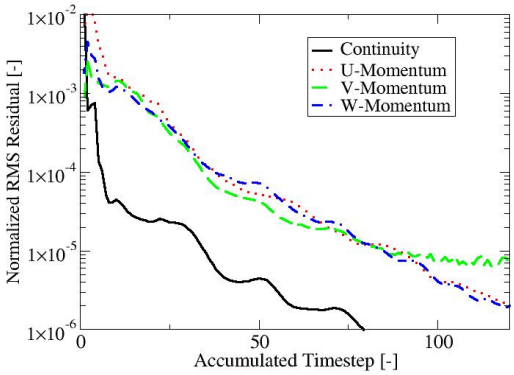

Figure 11: Convergence plot for medium grid for forward-swept wing.

Convergence for the medium grid can be seen in Figure 11 and Figure 12, which show the residual convergence and the convergence of the lift force for an angle of attack of α=20°.

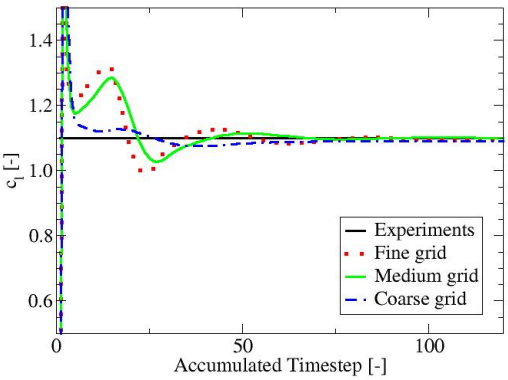

Figure 12: Convergence of lift coefficient c_l for three different grids for forward-swept wing test case (α=20°).

Figure 13 shows a comparison of the computed drag polar with the experiments using the SST turbulence model for the three different grids. Surprisingly, even the coarsest grid gives already quite accurate results for this case. On the finest grid, the simulations are in close agreement with the experimental data.

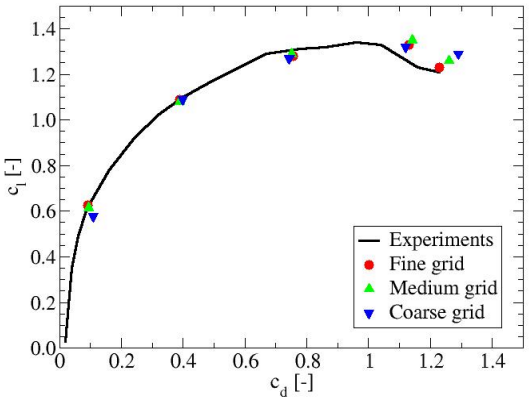

Figure 13: Comparison of drag polar for forward-swept wing on three different grids.

4.2 Flow over transonic DLR-F6 configurations

The DLR-F6 wing-body (WB) and wing-body-pylon nacelle (WBNP) have been test cases at the 2003 AIAA Drag Prediction workshop. For the workshop the test cases have been investigated independently by numerous groups. Details on the CFX simulations can be found in [23]. In the present context, the test case serves to demonstrate the numerical performance of the code for a complex transonic flow simulation. The flow conditions for these cases were: Ma=0.75, $Re=3x10^6$, α=-3°-2°.

Figure 14 shows the geometry of the WB test case. Several grids have been used for the test case. The results shown here are for the medium grid with $5.8x10^6$ nodes. The near wall spacing is around $y^+=1$ with average surface cell aspect ratios of the order of 10^4.

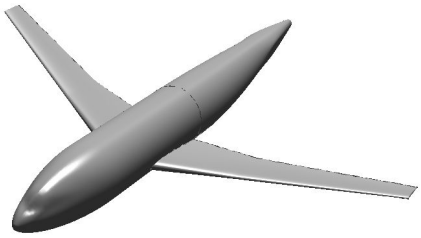

Figure 14: Geometry of DLR-F6 wing-body (WB) test case.

Figure 15 shows a typical residual convergence for the test case for α=-1°. It was observed that no full convergence in the residuals could be achieved, due to a slight transient oscillation of the corner separation zones at the wing-body intersection. Most other participants at the AIAA workshop observed a similar behavior.

Despite the incomplete convergence in the residuals, Figure 16 shows a good convergence of the forces for the same conditions. Note that even the relatively low lift force converges within ~100 iterations.

Figure 17 shows a comparison of the predicted and the experimental drag polar for the WB and the WBNP test case. The agreement with the experimental data is generally good over the entire angle of attack range. It is expected that further improvements for the WBNP case could be achieved by further grid refinement, as indicated in [23].

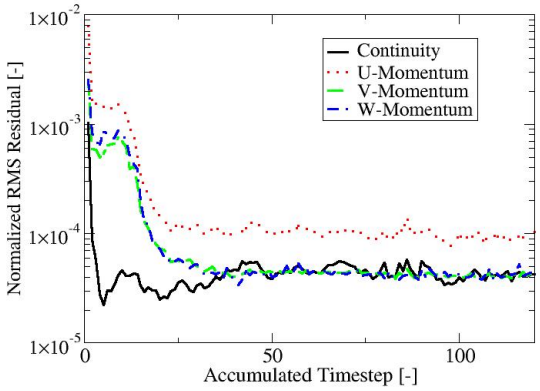

Figure 15: Residual convergence for DLR-F6 WB test case (medium grid, α=-1°).

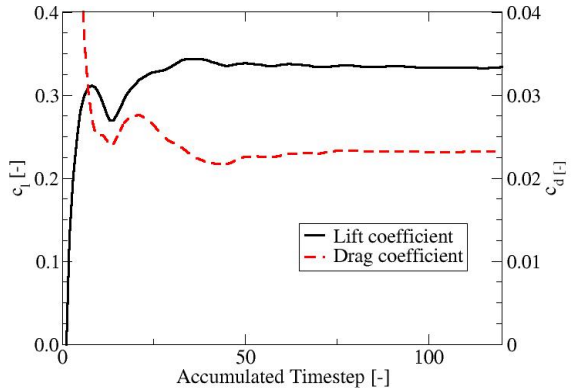

Figure 16: Force convergence for the DLR-F6 WB test case (medium grid, α=-1°). Left scale - lift. Right scale - drag.

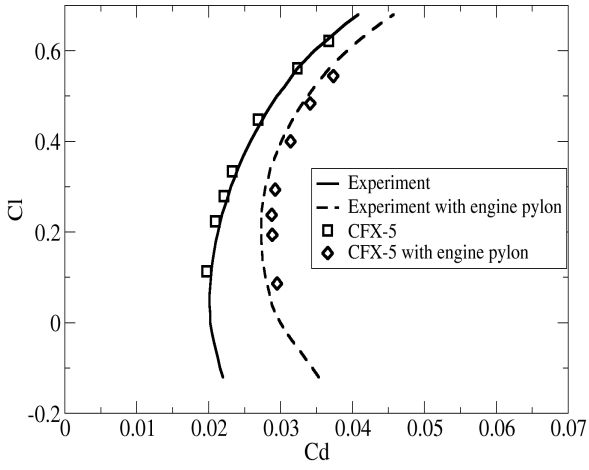

Figure 17: Drag polars for DLR-F6 WB and WBNP test cases. Comparison of numerical and experimental results.

Figure 18 shows pressure distributions at two different spanwise locations on the wing for the WBPN case also in good agreement with the experimental data. More details can also be found in [23].

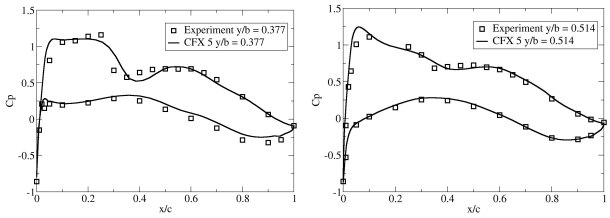

Figure 18: Measured and calculated pressure coefficient (Cp) at y/b = 0.377, y/b = 0.514 span for the DLR-F6 configuration with (WBNP) engine pylons.

4.3 Flow over a space vehicle configuration

The objective of this test case was to provide insight into the base flow physics and to evaluate the basic aerodynamics of a subscale (1 to 40) generic atmospheric entry space probe, especially drag and dynamic stability. Computations were performed over Mach numbers ranging between 0.8 and 2.6 and for angles of attack up to 8°. Due to axial symmetry, grids were generated for a 180° arc of the model. Solutions were marched from free-flight initial conditions until final converged solutions were obtained.

A schematic of the geometry is shown in Figure 19.

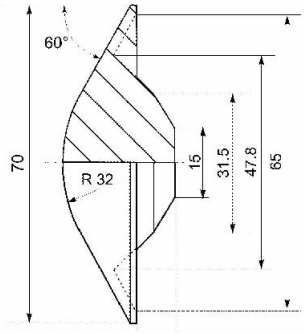

Figure 19: Geometry of entry space probe.

The convergence behavior of the momentum equations are shown in Figure 20 for M=2.6 and α=3°. It can be seen that the prediction converged in approximately 230 iterations to a normalized RMS residual of

below 10^{-5}. The forces are already constant after about 130 iterations (not shown).

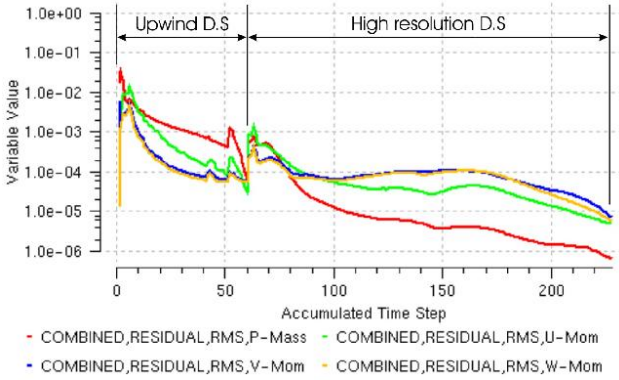

Figure 20: Convergence of momentum equations for atmospheric entry probe.

The predicted Mach number distribution around the model is shown in Figure 21 for M=2.6 and α=3°. The computations give a faithful representation of the flow field whose main features are remarkably well predicted if compared with a shadowgraph also shown in Figure 21. It clearly shows the detached bow shock, the shoulder expansion at the tip corner, the mixing layer characterized by large velocity gradients and the large recirculating region behind the base.

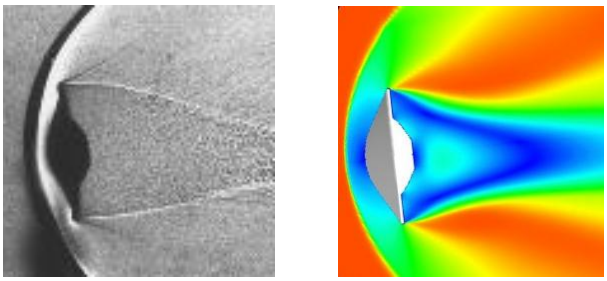

Figure 21: Left - Free Flight shadowgraph. Right - Mach number distribution around the entry probe (M=2.6, α=3°).

Forces and moments acting on the body were calculated by integration of the pressure and viscous force components. Figure 22 shows a comparison of experimental free flight aerodynamic coefficients as a function of angle of attack with those obtained numerically for a Mach number of 1.997. In all predicted cases, the average difference between CFD and free flight results was calculated to be 1.6% for CA, 2.1% for CN and 4.9% for Cm.

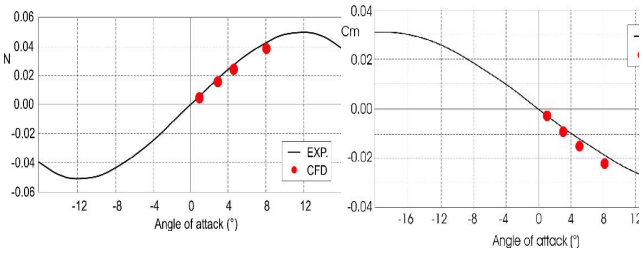

Figure 22: Left – Normal force vs. α°. Right – Moment vs.α°.

5. Conclusions

An overview of the numerical formulation of the general-purpose industrial CFD code CFX-5 was given. The emphasis of the presentation was on the formulation of the method for different Mach number regimes.

Several test cases have been shown demonstrating the ability of the method to handle generic and complex test cases from incompressible to high supersonic speeds.

Acknowledgement

Part of this work was supported by research grants from the European Union under the FLOMANIA project (Flow Physics Modelling - An Integrated Approach) The project is funded by the European Union and administrated by the CEC, Research Directorate-General, Growth Programme, under Contract No. G4RD-CT2001-00613.

References

[1] Jameson, A., Schmidt, W. and Turkel, E, Numerical solutions of the Euler equations by finite volume methods using Runge-Kutta time-stepping schemes, *AIAA Paper 81-1259*, 1981.

[2] Harten, A., High resolution schemes for hyperbolic conservation laws, *J. Comput. Physics*, 49, 1983.

[3] Radespiel, R and Kroll, N. Accurate flux vector splitting for shocks and shear layers. *J. Comput. Physics*, 121, 1995.

[4] Ferziger, J. H. and Peric, M. *Computational Methods for Fluid Dynamics.* Springer, 1997.

[5] Rhie C.M. and Chow, W.L. A numerical study of the turbulent flow past an isolated airfoil with trailing edge separation. *AIAA J.* 21, 1983.

[6] Raithby G.D., Schneider, G.E. Numerical solution of problems in incompressible fluid flow: treatment of the velocity-pressure coupling. *Numer. Heat Transfer*, 2, 1979.

[7] Van Doormaal J.P, Raithby G.D., Enhancement of the SIMPLE method for predicting incompressible

fluid flows, *Num. Heat Transfer*, Vol.7, pp147-163, 1984.

[8] Lee, D., v. Leer B. and Lynn, J.F. A local Navier-Stokes preconditioner for all Mach and cell Reynolds numbers. *AIAA Paper 97-2024*, 1997.

[9] Turkel, E., Vatsa, V.N. and Radespiel, R. Preconditioning methods for low-speed flows. *AIAA Paper 96-2460*, 1996.

[10] Spalart, P.R. and Allmaras, S.R., 1994,: A one-equation turbulence model for aerodynamic flows, *La Recherche Aerospatiale, No. 1, pp. 5-21*

[11] Menter, F.R. Two-equation eddy-viscosity turbulence models for engineering applications. *AIAA-Journal, 32(8)*, 1994.

[12] Raw, M., *A New Control-Volume Based Finite Element Procedure for the Numerical Solution of the Fluid Flow and Scalar Transport Equations*, Ph.D. Thesis, University of Waterloo, Canada, 1985.

[13] Huebner, K.H. *The Finite Element Method for Engineers*, John Wiley & Sons, 1975.

[14] Barth, T.J., Jesperson, D.C., The Design and Application of Upwind Schemes on Unstructured Meshes, *AIAA Paper 89-0366*, 1989.

[15] B.R. Hutchinson and G.D. Raithby, A Multigrid method based on the Additive Correction Strategy, *Numerical Heat Transfer*, Vol.9, pp. 511-530, 1986.

[16] M. Raw, Robustness of Coupled Algebraic Multigrid for the Navier-Stokes Equations, *AIAA Paper 96-0297, AIAA 34th Aerospace Sciences Meeting and Exhibit, Reno*, NV, 1996.

[17] Brandt, A., Diskin, B. and Thomas, J., Multigrid Efficiency for Computational Fluid Dynamics Simulations, *AIAA Paper 2001-2570, AIAA Computational Fluid Dynamics Conference*, Anaheim, CA, June 11-14, 2001

[18] Delery, J., Panaras A.G., Shock wave/boundary layer interaction in high-Mach-number flows, in Hypersonic experimental and computational capability, improvement and validation, *Vol. 1, AGARD AR 319*, 1996.

[19] Menter, F. R., Langtry, R. , Likki, S.R., Suzen, Y.B. and Huang, P.G., A correlation based transition model using local variables – Part I Model formulation, *Proc. ASME Turbo Expro* 2004, Vienna.

[20] Breitsamter, C., Vortex-Dominated Flowfields at Forward Swept Wing Configuration, *DGLR Jahrestagung München*, 1997.

[21] Breitsamter, C. and Laschka, B., Vortical Flowfield Structure at Forward Swept Wing Configurations, *ICAS Proceedings, 21st Congress*, Melbourne, 1998.

[22] Haase, W., Personal communication, 2004

[23] Langtry, R., Kuntz, M. and Menter, F.R., Drag prediction of engine-airframe interference effects with CFX-5. *AIAA Paper 2004-0391*, 2004.